Approximation of piecewise smooth functions and images by edge-adapted (ENO-EA) nonlinear multiresolution techniques

Francesc Arandiga, Albert Cohen, Rosa Donat, Nira Dyn and Basarab Matei

Abstract

This paper introduces and analyzes new approximation procedures for bivariate functions. These procedures are based on an edge-adapted nonlinear reconstruction technique which is an intrinsically two-dimensional extension of the essentially non-oscillatory and subcell resolution techniques introduced in the one dimensional setting by Harten and Osher. Edge-adapted reconstructions are tailored to piecewise smooth functions with geometrically smooth edge discontinuities, and are therefore attractive for applications such as image compression and shock computations. The local approximation order is investigated both in L^p and in the Hausdorff distance between graphs. In particular, it is shown that for general classes of piecewise smooth functions, edge-adapted reconstructions yield multiscale representations which are optimally sparse and adaptive approximations with optimal rate of convergence, similar to curvelets decompositions for the L^2 error.

1. Introduction

1.1 Background and motivation

Multiscale representations of images into wavelet bases have been successfully applied in applications such as compression and denoising. In these applications, one essentially takes advantage of the *sparsity* of the representation $f = \sum d_\lambda \psi_\lambda$, i.e. the concentration of the energy of the image f on a small number of coefficients d_λ. The detailed analysis of such methods, e.g. in [21], [28] and [15], demonstrates that their performances are directly related to a mathematical measure of the sparsity which can be given by two equivalent statements:

(i) The coefficient sequence (d_λ) is in $w\ell^p$: for all $\eta > 0$,

$$\#\{\lambda \; ; \; |d_\lambda| \geq \eta\} \leq C\eta^{-p}. \tag{1}$$

(ii) The nonlinear best N-term approximation f_N obtained by keeping the N largest $|d_\lambda|$ satisfies

$$\|f - f_N\|_{L^2} \leq CN^{-s} \quad , \quad s = \frac{1}{p} - \frac{1}{2} \tag{2}$$

We also refer to [14, 18] for a general treatment of nonlinear wavelet approximation. In recent years, it has been however observed that such approximations are sub-optimal with respect to edges, in the sense that they essentially perform an isotropic refinement which does not take advantage of their geometric smoothness. This is reflected by the deceiving rate of best N-term approximation $\|f - f_N\|_{L^2} \leq CN^{-\frac{1}{2}}$ (or equivalently the coefficient sequence is in $w\ell^1$) when $f = \chi_\Omega$ with $\partial\Omega$ arbitrarily smooth.

This intrinsic limitation has motivated new directions of research toward compact representation of geometry:

- Adaptive anisotropic triangulations obtained by thinning algorithms, which consists in a greedy point removal based on an error criterion such as in [17], or by adaptive refinement algorithm based on normal meshes such as in [8].
- Bases or frames with more anisotropic directional selectivity, such as curvelets [10, 11] and contourlets [20].
- Bandlets transforms [26, 27] which are based on tensor product of wavelet bases combined with local warping operators adapted to the edge of the image.
- Edgeprints approximations [9] consisting in wavelet expansions in which certain coefficients are replaced by their value associated to a wedge function which locally fits the image.

This paper is concerned with the analysis of geometric representations which retain the multiscale structure of wavelet decompositions, while incorporating at the same time a specific nonlinear treatment of edges *within the transformation process*. This idea was initially proposed in 1D by Ami Harten who introduced in [24, 25] a discrete multiresolution framework which allows to apply essentially non-oscillatory (ENO) and subcell resolution (ENO-SR) techniques (initially introduced in the context of numerical shock computation) within the decomposition and reconstruction process. In turn, these new transforms cannot be viewed as change of basis, similar to the more recent work in [6, 7]. A closely related approach introducing a concept of data-dependent ENO-wavelet basis was developed in [13]. These ideas have recently been applied to image compression, in [2] and [1], following a tensor product approach, which leads to the presence of artifacts near to the edges. An intrinsically bidimensional approach was proposed in [4, 29] which allows us to remove these artifacts. The goal of the present paper is to develop a rigorous mathematical analysis of this approach.

1.2 Harten's multiresolution framework

In a nutshell, the framework of Harten can be described as follows: we start from a finite set $f^J = (f_k^J)$ of discrete data sampled at the resolution 2^{-J}. For all j, we are given a decimation operator D_j^{j-1} which extracts from (f_k^j) the

discrete data (f_k^{j-1}) at the next coarser level, and a prediction operator P_{j-1}^j which produces an approximation of (f_k^j) from (f_k^{j-1}). These operators are constructed so to satisfy the consistency condition

$$D_j^{j-1} P_{j-1}^j = I. \tag{3}$$

We can represent f^j in terms of (f^{j-1}, e^{j-1}), where $e^{j-1} = f^j - P_{j-1}^j f^{j-1}$ is the prediction error. This new representation of f^j is redundant, since e^{j-1} belongs to the null space of D_j^{j-1} according to (3). This redundancy can be eliminated by representing e^{j-1} in terms of a basis of this space, which result in the detail vector d^{j-1}. Therefore we can represents f^j by (f^{j-1}, d^{j-1}). By iterating this procedure from level J to level $j = 0$ we obtain the multiscale representation of

$$f^J \leftrightarrow (f^{J-1}, d^{J-1}) \leftrightarrow (f^{J-2}, d^{J-2}, d^{J-1}) \leftrightarrow \cdots \leftrightarrow (f^0, d^0, ..., d^{J-1}). \tag{4}$$

In the present paper we shall restrict to the particular setting where f^j is thought as the cell-average discretization of an integrable function $f(t)$ at resolution 2^{-j} which fixes once and for all the decimation operator: in the one dimensional case

$$f_k^j := 2^j \int_{I_k^j} f \ \text{ and } \ f_k^{j-1} := \frac{1}{2}(f_{2k}^j + f_{2k+1}^j), \tag{5}$$

with $I_k^j := [2^{-j}k, 2^{-j}(k+1)]$ and in the two dimensional case

$$f_{k,l}^j := 2^{2j} \int_{C_{k,l}^j} f \ \text{ and } \ f_{k,l}^{j-1} := \frac{1}{4}(f_{2k,2l}^j + f_{2k+1,2l}^j + f_{2k,2l+1}^j + f_{2k+1,2l+1}^j), \tag{6}$$

with $C_{k,l}^j := I_k^j \times I_l^j$.

The choice of the prediction operator is now crucial, and should typically be guided by the objective of minimizing the prediction error over a class of signals and images of interest, in order to obtain multiscale representations which are as sparse as possible. The purpose of introducing nonlinearly data dependent prediction operators, such as *essentially non-oscillatory* (ENO) reconstructions as proposed in [24, 25], is to improve the prediction near the jumps or singularities of the data, while linear method classically generate large errors and spurious oscillations (Gibbs phenomenon). We next describe these ideas in the one-dimensional setting.

1.3 Non-linear 1D reconstruction techniques

The prediction operators proposed by Harten are based on a *reconstruction procedure*: from f^j, we reconstruct a function $\mathcal{R}_j f^j$ of the continuous variable which agrees with the discrete data in the sense that

$$2^j \int_{I_k^j} \mathcal{R}_j f^j = f_k^j \ \text{ for all } k, \tag{7}$$

and we next define the prediction $\hat{f}^{j+1} := P_j^{j+1} f^j$ according to

$$f_k^{j+1} := 2^{j+1} \int_{I_k^{j+1}} \mathcal{R}_j f^j. \tag{8}$$

Note that this always ensures the validity of the consistency property (3). The accuracy of the prediction operator is therefore tied to the accuracy of the reconstruction, namely the closeness of $\mathcal{R}_j f^j$ to f.

We are thus facing the general problem of accurately reconstructing a function f from its cell-average data at some scale $h > 0$ (with $h = 2^{-j}$ in our multiscale setting),

$$f_k := h^{-1} \int_{I_k} f, \;\; I_k := [kh, (k+1)h], \tag{9}$$

and we denote by $\mathcal{R}_h$ the reconstruction operator now viewed as an approximation operator acting on the function f (by averaging followed by reconstruction). A standard choice is to define $\mathcal{R}_h$ as a piecewise polynomial function:

$$\mathcal{R}_h f(t) = p_k(t) \;\; t \in I_k \tag{10}$$

where p_k is a polynomial of degree $2m$ which agrees with f on the centered stencil $S_k := \{k-m, \cdots, k+m\}$:

$$h^{-1} \int_{I_{k+l}} p_k = f_k, \;\; l = -m, \cdots, m. \tag{11}$$

The degree of the polynomials determines the order of accuracy: if $f \in C^s$ then the error $\|f - \mathcal{R}_h f\|_{L^\infty}$ behaves like $\mathcal{O}(h^r)$ with $r = \min\{s, 2m+1\}$ and more generally if $f \in W^{s,p}$ then $\|f - \mathcal{R}_h f\|_{L^p}$ behaves like $\mathcal{O}(h^r)$ with $r = \min\{s, 2m+1\}$. On the other hand, the presence of an isolated jump discontinuity of f at a point x deteriorates the local approximation order into $\mathcal{O}(1)$ on the $2m+1$ intervals I_k such that $x \in I_{k+l}$ for some $l \in \{-m, \cdots, m\}$ and also results into spurious oscillations (Gibbs phenomenon) in the vicinity of x.

Essentially Non-Oscillatory (ENO) techniques have been designed to remedy in part to this drawback. For this purpose, one typically introduces a measure of the oscillation of the discrete data on the stencil S_k. For each k, we select among all the stencils $\{S_{k-m}, \cdots, S_{k+m}\}$ which contain I_k the stencil $\tilde{S}_k$ which minimizes the chosen measure of oscillation. The ENO interpolant is then given by

$$\mathcal{R}_h f(t) = \tilde{p}_k(t), \;\; t \in I_k, \tag{12}$$

where $\tilde{p}_k$ is the polynomial which agrees with f on the stencil $\tilde{S}_k$. In comparison with the linear reconstruction based on the centered stencil, the approximation $\mathcal{R}_h$ based ENO reconstruction is a nonlinear operator with the same order of accuracy and it reduces the effect of an isolated jump singularity, since the

selected stencil will tend to avoid it. We therefore expect that the precision only deteriorates on the interval which contains the singularity.

The goal of the Subcell Resolution (ENO-SR) technique is to improve the approximation properties of the reconstruction even on this interval. It is based on a detection mechanism which labels as B (bad) an interval I_k which is suspected to contain a singularity, in the sense that the selected stencils for its immediate neighbors tend to avoid it. Thus I_k is B if $\tilde{S}_{k-1} = S_{k-m-1}$ and $\tilde{S}_{k+1} = S_{k+m+1}$. Other intervals are labeled as G (good). On a G interval I_k, we use the above described ENO reconstruction to define $\mathcal{R}_h f$. On a B interval I_k, we define $\mathcal{R}_h f$ as a piecewise polynomial

$$\mathcal{R}_h f(x) = q_k(t) := \tilde{p}_{k-1}(t) \text{ if } t \leq y, \ \tilde{p}_{k+1}(t) \text{ if } t \geq y, \tag{13}$$

where the jump point y is estimated by solving the algebraic equation

$$h^{-1} \int_{I_k} q_k = f_k. \tag{14}$$

In the case where there is not a unique solution y located inside I_k the interval is relabeled as G and the ENO reconstruction is used.

An intuitive statement is that ENO-SR reconstruction has an improved order of accuracy over the linear reconstruction for piecewise smooth functions. In a recent work [3], we proposed a rigorous analysis of the ENO-SR procedure (both for point-value and cell-average sampling) that made this statement more precise: for a function f with s uniformly bounded derivatives on $\mathbb{R} - \{\mathrm{x}\}$ and a jump discontinuity of height $|[f]|$ at x, we proved that the singularity is always detected for h smaller than a *critical scale*

$$h_c := \frac{|[f]|}{4 \sup_{t \in \mathbb{R} - \{\mathrm{x}\}} |f'(t)|}, \tag{15}$$

with accuracy $|x - y| \leq C h^{s+1}$. Intuitively, this critical scale represents the minimal level of resolution needed to distinguish between the jump and a smooth region with possibly high gradient. This allowed to establish the expected improvement of the rate of convergence of $\mathcal{R}_h f$ towards f in the L^p norm for $p < \infty$, as well as in the metric

$$d(f, g) = d_H(G_f, G_g) \tag{16}$$

with $G_f := (x, f(x))_{x \in \mathbb{R}}$ and $G_f := (x, g(x))_{x \in \mathbb{R}}$ the graphs of f and g and

$$d_H(A, B) := \sup_{x \in A} \inf_{y \in B} |x - y| + \sup_{x \in B} \inf_{y \in A} |x - y|, \tag{17}$$

the Hausdorff distance between sets. This metric is a natural substitute to the L^∞ norm for piecewise smooth functions with isolated jumps. In order to obtain these results, the ENO-SR procedure had to be slightly modified from its original conception in order to avoid the situation where a B interval which was detected by a false alarm in a region where f is smooth might be too close to another B interval which really contains a singularity, in which case the reconstruction on the first B interval by (13) might be using polynomials built from stencils which include the singularity. This issue will also be of importance in this paper.

1.4 Objectives and outline of the paper

Our paper is concerned with a genuinely two-dimensional extension of the ENO-SR procedure, which was firstly introduced in [29] and [4]. We refer to this approach as Edge-Adapted reconstruction (ENO-EA), since its goal is to accurately capture the geometrical edges from the cell-average data. Similar to the one dimensional ENO-SR procedure, a nonlinear operator $\mathcal{R}_h$ is defined which maps the cell-average data

$$f_{k,l} := h^{-2} \int_{C_{k,l}} f, \;\; C_{k,l} := I_k \times I_l, \tag{18}$$

to a piecewise polynomial function $\mathcal{R}_h f$. While in the one-dimensional case, the ENO-SR procedure estimates the location of a jump point within the cells that might contain one, the ENO-EA is based on estimating a line edge in the cells that might be crossed by an edge. This procedure is by far more complex since one needs to estimate both the location and orientation of the edge. A first version of the ENO-EA reconstruction procedure was introduced earlier in [29] in the particular case of bi-quadratic polynomial reconstruction, but despite its general good behavior with respect to edges, this procedure does not lead to optimal approximation results, due to the possibilities of "false alarms" in the detection of edges singularities. In this paper, we introduce a more elaborate version of ENO-EA reconstruction that circumvents these difficulties. This new procedure can be defined for piecewise polynomial reconstruction of any degree. More precisely we shall use polynomials of global degree $2m$, i.e. of the type

$$p(x,y) = \sum_{\alpha_x,\alpha_y \leq 2m} a_\alpha x^{\alpha_x} y^{\alpha_y}, \tag{19}$$

where $m > 0$ is arbitrary but fixed.

We describe in §2 the detection-selection mechanism which labels the various cells as singular or regular, and in §3 the reconstruction procedure which is operated on these different cells. Our approach to understanding the properties of these procedures with respect to an edge singularity is essentially a perturbation analysis between their behavior with respect to a line edge with piecewise constant values from both side and to the real curved edge. This analysis allows us to derive various approximation results in §4 for piecewise smooth functions with piecewise smooth edges. In particular, it is shown that the multiscale coefficients are in $w\ell^{\frac{2}{3}}$ (similar to curvelet coefficients) and that optimal rates of approximation can be obtained in L^p and in the Haudorff distance between graphs (16) by an adaptive multiscale method based on ENO-EA reconstruction. Some numerical tests are performed in §5 which illustrate these rates of approximation.

2. The detection and selection mechanism

2.1 Step images vs. piecewise smooth images

The edge-adapted reconstruction procedure is based on a detection and selection mechanism. The first step of detection generates a set of cells which are suspected to be crossed by an edge. The next selection steps remove certains cells of this set in order to eliminate the problems generated by false alarms. Our main point will be to show that all edges are detected and well reconstructed for h less than some critical scale h_c, similar to the analysis performed in [3] for the ENO-SR method.

Our analysis is based on first understanding the behavior of the procedure on a *step image*, by which we mean a two-dimensional function g of the type

$$g := g_+ \chi_{H^+} + g_- \chi_{H^-}, \tag{20}$$

where H^+ and H^- are two complementary half-plane separated by a line L. In all the following shall systematically denote by

$$\delta := |g_+ - g_-|, \tag{21}$$

the amplitude of the jump for such a function. The behavior of the procedure for more general piecewise smooth image with jump discontinuities on curved edges is then derived by a perturbation analysis. This type of reasoning will be detailed for the first results of the next section and sketched more briefly for the next results in order to limitate the length of the paper. Throughout our analysis C will always denote a generic constant which may vary even inside a chain of inequality, and whose dependence on the various parameters will be specified when this is relevant.

Assume that f is a piecewise C^1 function with a jump discontinuity on an edge curve E of C^2 smoothness. We denote by $\gamma(t)$ the arclength parametrization of E. The ENO-EA reconstruction procedure defines on each cell $C_{k,l}$ a reconstructed function $\mathcal{R}_h f$ which depends on the cell-average data on a set of neighboring cells

$$I_{k,l} = \{C_{k',l'} \ ; \ \max\{|k-k'|, |l-l'|\} \leq M\}, \tag{22}$$

where M is fixed and depends on the degree $2m$ of the polynomials that we use. We call $I_{k,l}$ the *influence set* of $C_{k,l}$, and for notational simplicity we identify it with the spatial domain obtained by taking the union of its $(2M+1)^2$ cells. We also define

$$E_{k,l} = \{t \ ; \ \gamma(t) \in I_{k,l}\}, \tag{23}$$

the set of values of t for which the edge curve crosses the set $I_{k,l}$ If $I_{k,l}$ is crossed by the edge, we can define a step image g by taking for L the tangent line to the edge at a point $(x_0, y_0) \in I_{k,l}$ and g_+ and g_- the limit values of f at this point from both side of the edge, as illustrated on Figure 1 (a). We also consider the intermediate image $\tilde{f}$ which has the same edge discontinuity E as f, but with constant values a and b from both side of this edge.

For (k', l') such that $\max\{|k - k'|, |l - l'|\} \leq M$, we have on the one hand the estimate

$$|f_{k',l'} - \tilde{f}_{k',l'}| \leq Ch \sup_{I_{k,l} \setminus E} |\nabla f|, \tag{24}$$

which accounts for the first order variation of the real image with respect to the constants g_+ and g_-, with $C = (M + 1)\sqrt{2}$. On the other hand, we also have

$$|g_{k',l'} - \tilde{f}_{k',l'}| \leq Ch\delta \sup_{E_{k,l}} |\gamma''(t)|, \tag{25}$$

which accounts for the second order variation of between the curved edge E and the line L, with $C = (M + 1)^2$. Here, it is assumed that this set is a single interval, in other words that there is no re-entrance of the curve in $I_{k,l}$ as illustrated on Figure 1 (b). This assumption should be viewed as similar to the assumption used in the one-dimensional setting that the jump point are separated by enough cells so that they can be discriminated by the ENO-SR procedure. Combining (24) and (25), we therefore obtain

$$|f_{k',l'} - g_{k',l'}| \leq Ch\Big(\sup_{I_{k,l} \setminus E} |\nabla f| + \delta \sup_{E_{k,l}} |\gamma''(t)| \Big), \tag{26}$$

an estimate which will play a key role in our analysis. The detection, selection and edge reconstruction procedures that we shall develop are both meant to be *exact* with respect to step images and *robust* with respect to the local perturbation expressed by (26).

Figure 1: (a) approximation of an edge by a line (b) forbidden situation

2.2 Detection

We introduce the following detection mechanism based on the first order finite difference:

1. If $|f_{k+1,l} - f_{k,l}| > |f_{k+n+1,l} - f_{k+n,l}|$ for all $n = -2m-2, \cdots, -1, 1, \cdots, 2m+2$, then $C_{k,l}$ and $C_{k+1,l}$ are labeled horizontally bad (HB).

2. If $\min\{|f_{k+1,l} - f_{k,l}|, |f_{k,l} - f_{k-1,l}|\} > |f_{k+n+1,l} - f_{k+n,l}|$ for all $n = -2m - 3, \cdots, -2, 1, \cdots, 2m + 2$ then $C_{k-1,l}$, $C_{k,l}$ and $C_{k+1,l}$ are labeled horizontally bad (HB).

This mechanism therefore generates pairs or triplets of adjacent HB cells. Other cells are labeled horizontally good (HG). It is readily seen that there always exists at least $2m+1$ consecutive HG cells between pairs or triplets of HB cells. This property will be important to avoid that false alarms are situated too close to an edge, although more will be needed as explained in §2.5.

We perform a similar mechanism based on the finite difference in the vertical direction, which labels the cells as VB or VG. Each cell has now two labels corresponding to its classification by the horizontal and vertical detection.

Our first result states that with such a mechanism, all the cells crossed by a line edge in a step image are detected either horizontally or vertically. We introduce the angle

$$\theta^* := \mathrm{Arctg}(\frac{2}{3}) < \frac{\pi}{4}, \tag{27}$$

which will be of critical importance in all the subsequent analysis.

Lemma 1 *Assume that g is a step image of the type (20) and let $\theta \in [0, \frac{\pi}{2}]$ be the angle between line L and the horizontal axis. If $|\theta| \geq \theta^*$ then all cells which are crossed by L are labeled HB. If $|\theta| \leq \frac{\pi}{2} - \theta^*$ then all cells which are crossed by L are labeled VB. Since $\theta^* < \frac{\pi}{4}$ all cells crossed by a line edge are detected horizontally or vertically or in both directions.*

Proof: We assume that $|\theta| \geq \theta^*$, the case $|\theta| \leq \frac{\pi}{2} - \theta^*$ being treated by similar arguments. Recall that δ is the amplitude of the jump in g. On a fixed row l of cell, the line L can cross at most 3 cells $C_{k,l}$, due to the limitation on its angle. We consider these three cases separately:
Case 1. Only $C_{k,l}$ is crossed by L. Then, we have $|g_{q+1,l} - g_{q,l}| = 0$ for $q \leq k-2$ and $q \geq k+1$. On the other hand, we have

$$|g_{k+1,l} - g_{k,l}| + |g_{k,l} - g_{k-1,l}| = \delta, \tag{28}$$

and therefore

$$|g_{k+1,l} - g_{k,l}| \geq \frac{\delta}{2} \text{ or } |g_{k,l} - g_{k-1,l}| \geq \frac{\delta}{2} \tag{29}$$

It follows that $C_{k,l}$ is always contained in a HB pair or triplet.
Case 2. Two cells $C_{k,l}$ and $C_{k+1,l}$ are crossed by L as illustrated on Figure 2. Then we have $|g_{q+1,l} - g_{q,l}| = 0$ for $q \leq k-2$ and $q \geq k+2$. It is easily checked that the sum of the areas of the two triangles defined by L in each of the two cell is smaller than half of the area of one cell. From this it follows that

$$|g_{k+1,l} - g_{k,l}| \geq \frac{\delta}{2}, \tag{30}$$

and therefore

$$|g_{k,l} - g_{k-1,l}| + |g_{k+2,l} - g_{k+1,l}| \leq \frac{\delta}{2}, \tag{31}$$

so that either $|g_{k,l} - g_{k-1,l}|$ or $|g_{k+2,l} - g_{k+1,l}|$ is less than $\frac{\delta}{4}$. It follows that $C_{k,l}$ and $C_{k+1,l}$ are necessarily a HB pair or inside a HB triplet.

Case 3. Three cells $C_{k-1,l}$, $C_{k,l}$ and $C_{k+1,l}$ are crossed by L. Then we have $|g_{q+1,l} - g_{q,l}| = 0$ for $q \leq k-3$ and $q \geq k+2$. Elementary, yet tedious, geometrical consideration show that the differences $|g_{k+2,l} - g_{k+1,l}|$ and $|g_{k,l} - g_{k-1,l}|$ respectively attain their maximal and minimal value $\frac{\delta}{12}$ and $\frac{\delta}{3}$ in the configuration which is displayed on Figure 3 which corresponds to the case where $\theta = \theta^*$ and the edge crosses the first cell only at its right corner. By symmetry, we have

$$\max\{|g_{k+2,l} - g_{k+1,l}|, |g_{k-1,l} - g_{k-2,l}|\} \leq \frac{\delta}{12}, \tag{32}$$

and

$$\min\{|g_{k+1,l} - g_{k,l}|, |g_{k,l} - g_{k-1,l}|\} \geq \frac{\delta}{3}. \tag{33}$$

It follows that $C_{k-1,l}$, $C_{k,l}$ and $C_{k+1,l}$ are necessarily a HB triplet. ◇

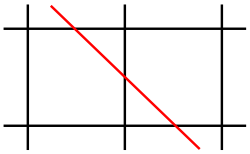

Figure 2: Crossing of two cells $C_{k,l}$ and $C_{k+1,l}$ by L

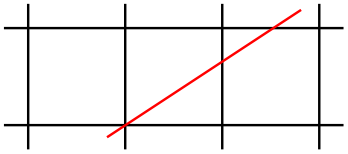

Figure 3: Extremal configuration of L crossing $C_{k-1,l}$, $C_{k,l}$ and $C_{k+1,l}$

Remark 1 *A consequence of the above lemma is that if a cell is crossed by L with $\theta^* \leq |\theta| \leq \frac{\pi}{2} - \theta^*$ then it should be labeled both HB and VB. In turn if a cell is labeled HB and VG (resp. VB and HG) and if it is crossed by L then we necessarily have $|\theta| > \frac{\pi}{2} - \theta^*$ (resp. $|\theta| \leq \theta^*$).*

Our next result will show that when the scale h is smaller than some critical scale h_c, the same detection properties hold for a piecewise smooth image f with a curved edge E. Assuming that the influence set $I_{k,l}$ of a cell $C_{k,l}$ is crossed by an edge E of arclength parametrization $\gamma(t)$, we define this critical scale h_c by

$$\frac{1}{h_c} := \frac{\sup_{I_{k,l} \setminus E} |\nabla f|}{\sup_{E_{k,l}} |[f](t)|} + \sup_{E_{k,l}} |\gamma''(t)|, \tag{34}$$

where the set $E_{k,l}$ has been defined by (23)

Lemma 2 *There exists a constant κ such that for $h \leq \kappa h_c$, the cell $C_{k,l}$ crossed by the curved edge E is labeled either HB or VB. More precisely, consider L the line which is tangent to E at the point which maximizes the jump $|[f]|(t)$ on $I_{k,l}$ and its angle θ with respect to the horizontal axis. If $|\theta| \geq \theta^*$ then $C_{k,l}$ is labeled HB. If $|\theta| \leq \frac{\pi}{2} - \theta^*$ then $C_{k,l}$ is labeled VB.*

Proof: Assume again without loss of generality that $|\theta| \geq \theta^*$ and define g the step image which takes on each side of L the corresponding limit values of f at the contact point. We remark that the condition $h \leq \kappa h_c$ is equivalent to

$$h\Big(\sup_{I_{k,l}\setminus E} |\nabla f| + \delta \sup_{E_{k,l}} |\gamma''(t)|\Big) \leq \kappa\delta, \tag{35}$$

where

$$\delta = \sup_{E_{k,l}} |[f](t)|. \tag{36}$$

Therefore, by (26), this means that

$$|f_{k',l'} - g_{k',l'}| \leq C\kappa\delta, \tag{37}$$

when $\sup\{|k-k'|, |l-l'|\} \leq M$. We then consider the same three cases as in the the proof of lemma 1. In the first case, we know that $|g_{q+1,l} - g_{q,l}| = 0$ for $q \leq k-2$ and $q \geq k+1$, and that

$$|g_{k+1,l} - g_{k,l}| \geq \delta/2 \ \text{ or } \ |g_{k,l} - g_{k-1,l}| \geq \frac{\delta}{2}. \tag{38}$$

Therefore, using (37), we obtain that

$$|f_{q+1,l} - f_{q,l}| \leq 2C\kappa\delta \tag{39}$$

for $q \leq k-2$ and $q \geq k+1$, and that

$$|f_{k+1,l} - f_{k,l}| \geq \frac{\delta}{2} - 2C\kappa\delta \ \text{ or } \ |f_{k,l} - f_{k-1,l}| \geq \frac{\delta}{2} - 2C\kappa\delta. \tag{40}$$

It follows that if κ is chosen small enough such that $8C\kappa < 1$, we reach the same conclusion that $C_{k,l}$ is always contained in a HB pair or triplet. The two other cases are treated by a similar perturbation approach. $\diamond$

Note that our proof actually shows that the whole bad pairs or triplets around $C_{k,l}$ coincide for f and g.

2.3 Selection of admissible configurations

As a second step, we perform a selection mechanism introducing the notion of admissible and non-admissible configuration.

Consider a HB pair or triplet $(C_{k,l})_{k_l^- \leq k \leq k_l^+}$. We say that this set of cell belongs to an admissible configuration if and only if there exists similar HB pairs or triplets $(C_{k,l+n})_{k_{l+n}^- \leq k \leq k_{l+n}^+}$ on the neighboring rows $|n| = 1, \cdots, m$,

such that two adjacent rows always have an HB cell at the same column. In other words, for all $p = l - m, \cdots, l + m - 1$, there exists a k such that we have jointly

$$k_p^- \leq k \leq k_p^+ \text{ and } k_{p+1}^- \leq k \leq k_{p+1}^+. \tag{41}$$

Of course a similar notion of admissible configuration is defined for VB pair, by exchanging the roles of rows and columns. An example of admissible and non-admissible configuration in the case $m = 2$ is presented on Figure 4.

The HB and VB cells which do not belong to an admissible configuration are relabeled HG and VG. Note that cells sharing the same pair or triplet always end-up with the same label.

Remark 2 *It is important to note that we do not perform the relabeling in an sequential way which would correspond to take into account the relabeling of the previous cells when examining a new cell. Instead, during the whole selection process, we keep in store all the labels HB and VB which were obtain after the initial detection step, and we relabel each individual cell simultaneously based on these initial labels.*

Figure 4: Admissible and non-admissible configurations

The next result states that the cells crossed by a line edge in a step image always belong to an horizontal or vertical admissible configuration.

Lemma 3 *Assume that g is a step image of the type (20) and let $\theta \in [0, \frac{\pi}{2}]$ be the angle between line L and the horizontal axis. If $|\theta| \geq \theta^*$ then all cells which are crossed by L belong to an admissible configuration of HB cells. If $|\theta| \leq \frac{\pi}{2} - \theta^*$ then all cells which are crossed by L belong to an admissible configuration of VB cells.*

Proof: Assume without loss of generality that $|\theta| \geq \theta^*$. Then, we have already seen that on each row, the cells which are crossed by the line L are labeled as HB. Such set of cells always satisfy the property (41) except in the non-generic case where L touches a corner between four cells as illustrated on Figure 5. In such a case however, the analysis in the proof of Lemma 1 shows that the four cells will be labeled as HB. Indeed, in this analysis a cell may still be considered to be crossed by the line edge even if it is only touched at its corner. This concludes the proof. ◇

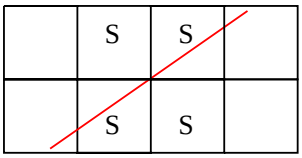

Figure 5: Case of a line edge touching a corner: the four S cells are detected

Obviously, the same perturbation analysis as in Lemma 2 allows to extend this result to piecewise smooth image f with a curved edge E.

Lemma 4 *There exists a constant κ such that for $h \leq \kappa h_c$, the cell $C_{k,l}$ crossed by the curved edge E is labeled either HB or VB and belong to an admissible configuration of similarly labeled cells. More precisely, consider L the line which is tangent to E at the point which maximizes the jump $|[f]|(t)$ on $I_{k,l}$ and its angle θ with respect to the horizontal axis. If $|\theta| \geq \theta^*$ then $C_{k,l}$ belong to an admissible configurations of HB cells. If $|\theta| \leq \frac{\pi}{2} - \theta^*$ then $C_{k,l}$ belong to an admissible configurations of VB cells.*

Proof: As in the proof of Lemma 2, we introduce the step image g and we obtain that for $h < \kappa h_c$ the bad pairs or triplets around $C_{k,l}$ and its neighboring rows coincide for f and g. ◇

2.4 Orientation test

The third step performs an orientation test on the cells which have been labeled both HB and VB after the selection step has been performed. Assume that $C_{k,l}$ is such a cell, we then define its vertical and horizontal gradient by

$$H_{k,l} := |f_{k+2,l} + f_{k+1,l} - f_{k-1,l} - f_{k-2,l}|,$$
$$V_{k,l} := |f_{k,l+2} + f_{k,l+1} - f_{k,l-1} - f_{k,l-2}|.$$

The orientation test simply consists in comparing those two quantities.

If $H_{k,l} < V_{k,l}$ the "vertical label" of $C_{k,l}$ is set to VG, and if $H_{k,l} \geq V_{k,l}$ the "horizontal label" of $C_{k,l}$ is set to HG. Therefore, after this test is performed, all the cells are either horizontally bad (HB-VG), vertically bad (HG-VB) or good (HG-VG). We therefore denote their simplified labels as HB, VB and G.

Our next result shows that a line edge is still detected after this third step and that the result of the test gives some information on its orientation.

Lemma 5 *Assume that g is a step image of the type (20) and let $\theta \in [0, \frac{\pi}{2}]$ be the angle between line L and the horizontal axis. Let $C_{k,l}$ belong to both a HB or VB pair or triplet one of which is crossed by L. Then if $|\theta| \leq \theta^*$, we then have $H_{k,l} < V_{k,l}$ and if $|\theta| \geq \frac{\pi}{2} - \theta^*$, then $H_{k,l} > V_{k,l}$.*

Proof: Without loss of generality we only consider the first case, namely $|\theta| \leq \theta^*$. Due to this angle condition, and the fact that $C_{k,l}$ belong to both a HB or VB

pair or triplet one of which is crossed by L, it is readily seen that L necessarily crosses one of the cells $C_{k,l-2}, \cdots, C_{k,l+2}$. Moreover, a simple computation shows that the segment of L which intersects the VB pair or triplet does not hit $C_{k,l-2}$ on its lower half part: otherwise, we would have $|g_{k,l} - g_{k,l-1}| = 0$ and $|g_{k,l-2} - g_{k,l-3}| \geq 3\delta/16$ so that $C_{k,l}$ could not be within a VB pair or triplet. Similarly, the segment of L which intersects the VB pair or triplet does not hit $C_{k,l+2}$ on its upper half part.

Under these limitations, elementary yet tedious geometrical consideration show that we always have

$$V_{k,l} \geq H_{k,l} + \frac{\delta}{24}, \tag{42}$$

the case of equality corresponding to the extremal configuration illustrated on Figure 6 where $\theta = \theta^*$ and L contains the center of the cell. $\diamond$

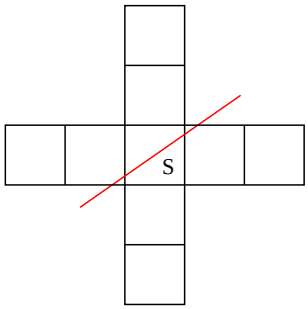

Figure 6: External configuration for the orientation test

Remark 3 *A simpler choice for the numerical gradients would be* $H_{k,l} := |f_{k+1,l} - f_{k-1,l}|$ *and* $V_{k,l} := |f_{k,l+1} - f_{k,l-1}|$. *The reason for involving two additional cells in the definition of* $H_{k,l}$ *and* $V_{k,l}$ *is the need for detecting the orientation of a line which passes through the singular pair or triplet containing the cell* $C_{k,l}$ *but not through* $C_{k,l}$ *itself.*

Again, the same perturbation analysis as in Lemma 2 allows to extend as follows this result to piecewise smooth image f with a curved edge E.

Lemma 6 *Let* $C_{k,l}$ *belong to both a HB or VB pair or triplet one of which is crossed by* E. *Consider* L *the line which is tangent to* E *at the point which maximizes the jump* $|[f]|(t)$ *on* $I_{k,l}$ *and let* $\theta \in [0, \frac{\pi}{2}]$ *be the angle between* L *and the horizontal axis. There exists a constant* κ *such that for* $h \leq \kappa h_c$, *if* $|\theta| \leq \theta^*$ *we then have* $H_{k,l} < V_{k,l}$ *and if* $|\theta| \geq \frac{\pi}{2} - \theta^*$ *then* $H_{k,l} > V_{k,l}$.

2.5 Testing the reconstruction stencils

Consider a cell $C_{k,l}$ which has been labeled HB after the the three previous steps (detection-configuration-orientation). We know that it is surrounded by an

admissible configuration of HB cells $(C_{k,l+n})_{k_{l+n}^- \leq k \leq k_{l+n}^+}$ for $|n| \leq m$ identified after the second selection step (some of these cells may actually be labeled VB after the third orientation step). We introduce the left and right reconstruction stencils

$$S_l := \{C_{k,l+n} \ ; \ k_{l+n}^- - 2m - 1 \leq k < k_{l+n}^-, \ \ |n| \leq m\}, \tag{43}$$

and

$$S_r := \{C_{k,l+n} \ ; \ k_{l+n}^+ < k \leq k_{l+n}^+ + 2m + 1, \ \ |n| \leq m\}. \tag{44}$$

These stencils are depicted on Figure 7 in the case $m = 1$. It is important to note that these stencils are connected domains due to the shape properties of admissible configurations. We shall see further that such stencils are unisolvent in the sense that their cell-average data defines a unique polynomial of global degree $2m$.

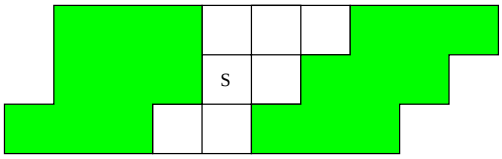

Figure 7: reconstruction stencils (in grey) for the HB cell S in the case $m = 1$

Of course, we define similar stencils in the upper and lower direction in the case of a cell which has been labeled VB after the three previous steps. Without loss of generality, we only consider in the following the case of an HB cell, the other case being treated by symmetry.

From the definition of the detection mechanism in §2.2, it is readily seen that all the cells in both right and left stencils surrounding the configuration have been labeled HG since the first detection step. However, some of them may have been labeled VB. In such a case, it is important that we understand it one of the stencil might be crossed by the edge, in which case we do not want to use it for the reconstruction. For this purpose, we introduce two quantities that will serve us to test the configuration and its surrounding stencil. The first quantity J_c is defined as the sum of the horizontal jumps inside the central HB pair or triplet of the configuration, namely

$$J_c := \sum_{k=k_l^-+1}^{k_l^+} |f_{k,l} - f_{k-1,l}|. \tag{45}$$

The second quantity J_s is defined as one half of the sup of the vertical jumps for each cell within the stencil. Since we have two stencils, we define for each of them

$$J_s^l := \frac{1}{2} \max_{C_{m,n} \in S_l} \max\{|f_{m,n+1} - f_{m,n}|, |f_{m,n} - f_{m,n-1}|\}, \tag{46}$$

and

$$J_s^r := \frac{1}{2} \max_{C_{m,n} \in S_r} \max\{|f_{m,n+1} - f_{m,n}|, |f_{m,n} - f_{m,n-1}|\}. \tag{47}$$

If a stencil, say S_l contains an VB cell, we compare J_s^l and J_c and relabel $C_{k,l}$ as G if $J_s^l > J_c$. Otherwise $C_{k,l}$ is maintained as HB.

The following result reveals that this test maintains the alarm on the cells which are indeed crossed by a line edge and eliminates the false alarms which are too close to a real alarm.

Lemma 7 *Assume that g is a step image of the type (20). If the line L crosses the HB pair or triplet containing $C_{k,l}$, then the following properties hold:*

(i) $|\theta| > \theta^*$,

(ii) L does not cross any cell of the stencils,

(iii) $J_c \geq \frac{5\delta}{8}$ and $\max\{J_s^l, J_s^r\} \leq \frac{\delta}{3}$.

Consequently, the HB label is maintained on $C_{k,l}$. On the other hand, if the line L crosses one of the stencils, say S_l, then the following properties hold:

(i) $|\theta| \leq \theta^*$,

(ii) L does not cross the HB pair or triplet containing $C_{k,l}$,

(iii) $J_c = 0$ and $J_s^l \geq \frac{\delta}{3}$.

Consequently $C_{k,l}$ is relabeled as G.

Proof: Assume first that L crosses the HB pair or triplet containing $C_{k,l}$. We show that we then have necessarily $|\theta| > \theta^*$. Indeed, assuming that $|\theta| \leq \theta^*$, elementary yet tedious geometrical considerations show that since L crosses the HB pair, it also crosses the vertical row containing $C_{k,l}$ in such a way that this cell was necessarily also labeled VB after the second configuration test. It was therefore relabeled HB after the third orientation test, which according to lemma 5 is in contradiction with $|\theta| \leq \theta^*$. As we already remarked, the cells in the stencil had to be labeled HG after the first detection test. Since $|\theta| > \theta^*$, this would be in contradiction with the fact that L crosses one them, according to lemma 1. Therefore, no cell of the stencil is crossed by L.

From this last fact and $|\theta| > \theta^*$, it is easily checked that $\max\{J_s^l, J_s^r\} \leq \frac{\delta}{3}$, the equality corresponding to the extremal case where L touches the corner of a cell in the stencil and $|\theta| = \theta^*$. Since L crosses the HB pair, elementary yet tedious geometrical considerations show that $J_c \geq \frac{5\delta}{8}$, the equality corresponding to the extremal case of a HB pair crossed symmetrically by L as on figure 2 and such that $|\theta| = \theta^*$.

Assuming next that L crosses one of the stencils. We then know that necessarily $|\theta| \leq \theta^*$ otherwise the cell which is crossed by L inside the stencil would have been labeled HB after the first detection test. As already shown above, if L was crossing the HB pair or triplet, $C_{k,l}$ would have been also labeled VB after the second configuration test, and it would have been relabeled HG after the third orientation test according to lemma 5. Therefore, L does not crosses the HB pair or triplet which clearly implies $J_c = 0$. On the other hand, it is easily checked that $\max\{J_s^l, J_s^r\} \geq \frac{\delta}{3}$, the equality corresponding to the extremal case where L touches the corner of a cell in the stencil and $|\theta| = \theta^*$. The proof of the lemma is thus complete. ◇

Again, the same perturbation analysis as in Lemma 2 allows to extend as follows this result to piecewise smooth image f with a curved edge E.

Lemma 8 *Let L be the line which is tangent to E at the point which maximizes the jump $|[f]|(t)$ on $I_{k,l}$ and θ its angle with respect to the horizontal axis. There exists a constant κ such that for $h \leq \kappa h_c$, the following results hold. If the edge E or the line L crosses the HB pair or triplet containing $C_{k,l}$, then the following properties hold:*

(i) $|\theta| > \theta^*$,

(ii) E and L do not cross any cell of the stencils,

(iii) $J_c > \max\{J_s^l, J_s^r\}$.

Consequently, the HB label is maintained on $C_{k,l}$. On the other hand, If the edge E or the line L crosses one of the stencils, say S_l, then the following properties hold:

(i) $|\theta| \leq \theta^*$,

(ii) E and L do not cross the HB pair or triplet containing $C_{k,l}$,

(iii) $J_c < J_s^l$.

Consequently $C_{k,l}$ is relabeled as G.

3. The reconstruction procedure

The various steps that we described so far have the effect of diminishing the number of HB and VB cells. According to our results, we are ensured that all cells crossed by an edge end up being labeled HB or VB under the condition $h \leq \kappa h_c$. In other words, we are ensured that if a cell $C_{k,l}$ is labeled G, it is not crossed by an edge unless $h \geq \kappa h_c$.

Our reconstruction procedure will therefore consist in building our polynomial functions from cell-average data on stencils which if possible only consists of G cells.

3.1 The reconstruction stencils

It is well-known that cell-average data on a $(2m+1) \times (2m+1)$ square stencil uniquely determines a polynomial of global degree $2m$. However, as already announced in the previous section, we might be led to use stencils which are not square shaped but of the more general type

$$S := \{C_{k+n,l} \ ; \ l_{k+n} \leq l < l_{k+n} + 2m + 1, \ \ |n| \leq m\}, \tag{48}$$

or

$$S := \{C_{k,l+n} \ ; \ k_{l+n} \leq k < k_{l+n} + 2m + 1, \ \ |n| \leq m\}. \tag{49}$$

In the following elementary lemma, we prove that cell-average data on such stencils also uniquely determine a polynomial of global degree $2m$.

Lemma 9 *There exists a unique polynomial of global degree $2m$ which agrees with a set of cell-average over a stencil S of the type (48) or (49).*

Proof: Since the stencil S has the correct cardinality $(2m+1)^2$, it suffices to show that a polynomial p of global degree $2m$ with null cell-averages over S is necessarily trivial. Without loss of generality, we consider the case of a stencil of the type (48). If p is a polynomial and $p_{k,l}$ denotes its cell-average on $C_{k,l}$, it is easily checked that

$$p_{k,l} = \tilde{p}(kh, lh), \tag{50}$$

with $\tilde{p}$ a polynomial of global degree $2m$ which has the same coefficients as p for the term of highest global degree. From the assumption that $p_{k,l} = 0$ when $C_{k,l} \in S$ we first derive that $\tilde{p}((k+n)h, t) = 0$ for all $t \in \mathbb{R}$ and $|n| \leq m$, which implies that $\tilde{p}$ is identically 0. Consequently p is also identically 0. $\diamond$

3.2 Reconstruction procedure on a non-singular cell

Consider a cell $C_{k,l}$ which is labeled G after the four steps of detection and selection which were described in §2. In such a cell the reconstruction $\mathcal{R}_h f$ will be defined as a single polynomial of global degree $2m+1$, which is constructed as follows.

We first consider the square stencil

$$S_{k,l} = \{C_{k+n,l+q}\ ;\ |n|, |q| \leq m\} \tag{51}$$

which is centered around $C_{k,l}$. In the case where this stencil only consists of G cells, we take for $\mathcal{R}_h f$ the unique polynomial p which agrees with the cell-average data over the stencil, that is such that

$$h^{-2} \int_{C_{k+n,l+q}} p(x,y)dxdy = f_{k+n,l+q}, \quad |n|, |q| \leq m. \tag{52}$$

In the case where this stencil contains one or more HB or VB cells, we need to select more carefully the reconstruction stencil. This situation typically occurs when $C_{k,l}$ corresponds to a smooth region which is located close to an edge. Our labeling procedure does not always ensure the existence of a square stencil containing $C_{k,l}$ consisting only of G cells, but we can still select a reasonable stencil by using a ENO-like strategy: we introduce the cost function defined by the sum of the vertical and horizontal jumps of the data inside the stencil, namely

$$\mathcal{C}(S_{k,l}) := \sum_{-m \leq n, q < m} (|f_{k+n+1,l+q} - f_{k+n,l+q}| + |f_{k+n,l+q+1} - f_{k+n,l+q}|) \tag{53}$$

and we select among the square stencils $(S_{k+n,l+q})_{|n|,|q| \leq m}$ which contain $C_{k,l}$ the one that minimizes this quantity (in the case of non-uniqueness of the minimizer, we systematically select the one with the smallest value of $|n| + |q|$ which has the effect of promoting the centered stencil). We then take for $\mathcal{R}_h f$ the unique polynomial p which agrees with the cell-average data over the selected stencil $\tilde{S}_{k,l}$.

3.3 Reconstruction procedure on a singular cell

Consider now a cell $C_{k,l}$ which was labeled HB or VB after the four steps of detection and selection which were described in §2. In such a cell the reconstruction $\mathcal{R}_h f$ will be defined as a piecewise polynomial function with a line edge discontinuity. Without loss of generality, we describe the construction of this function in the case of a HB label.

We first construct the line edge $L_{k,l}$ by considering the cell averages on the three row $\{l-1, l, l+1\}$. On each of these rows, we consider the HB pair or triplet which is contained in the admissible configuration of HB cells surrounding $C_{k,l}$ after the second selection step, and we use the cell-average data to identify the position of the line. Consider for example the central row l and the HB pair or triplet $(C_{q,l})_{q_l^- \leq q \leq q_l^+}$. With the notations

$$a := f_{q_l^- - 1, l}, \;\; b := f_{q_l^+ + 1, l} \;\text{ and }\; c := \frac{1}{q_l^+ - q_l^- + 1} \sum_{q_l^- \leq q \leq q_l^+} f_{q,l}, \tag{54}$$

we define the position

$$x_l := h\Big(q_l^- + \frac{(q_l^+ - q_l^- + 1)(c-b)}{a-b}\Big). \tag{55}$$

which corresponds the location of the discontinuity identified by the one-dimensional subcell resolution procedure: indeed it is such that the piecewise constant function $a\chi_{x \leq x_l} + b\chi_{x > x_l}$ agrees with the average c over the interval $[hq_l^-, h(q_l^+ + 1)]$ which corresponds to the HB pair or triplet. We define the point

$$z_l := (x_l, (l + \frac{1}{2})h), \tag{56}$$

which corresponds to the mid-point of the vertical segment crossing the row l at the position x_l. In a similar way, we define x_{l-1}, x_{l+1}, z_{l-1} and z_{l+1}. A key observation is the following:

In the case of a step image $g(x, y)$ the points $\{z_{l-1}, z_l, z_{l+1}\}$ are exactly located on the line L.

This is easily verified by geometrical reasoning: the one dimensional piecewise constant function $a\chi_{x \leq x_l} + b\chi_{x > x_l}$ has exactly average c over $[hq_l^-, h(q_l^+ + 1)]$ if and only if z_l coincides with the center of the segment of L crossing the row l since this is equivalent to saying that the two triangles defined by L from both side of the vertical segment at position x_l have the same area, as illustrated by figure 8. Note that in this reasoning we have used the fact that the line segment L only crosses the row l inside the HB pair or triplet, according to Lemma 5.

A natural way to build the line $L_{k,l}$ is therefore to find a line which matches the points $\{z_{l-1}, z_l, z_{l+1}\}$ (which are not necessarily aligned for cell-average data that do not come from a step image). A first possibility is simply to take two of

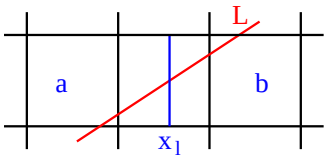

Figure 8: The point z_l is located on L for a step image.

these points and consider the line which connects them. For symmetry reasons, the natural choice is then to use $\{z_{l-1}, z_{l+1}\}$. Another possibility which uses the three points consists in finding the line by a minimization of the least-square deviation

$$D = |x_{l-1} - \tilde{x}_{l-1}|^2 + |x_l - \tilde{x}_l|^2 + |x_{l+1} - \tilde{x}_{l+1}|^2, \tag{57}$$

where $\{\tilde{x}_{l-1}, \tilde{x}_l, \tilde{x}_{l+1}\}$ are the horizontal positions of the centers of the segments of $L_{k,l}$ crossing the rows $l-1$, l and $l+1$. One last option consists in imposing that $L_{k,l}$ contains the point z_l and minimizing the least-square deviation

$$\tilde{D} = |x_{l-1} - \tilde{x}_{l-1}|^2 + |x_{l+1} - \tilde{x}_{l+1}|^2. \tag{58}$$

This last option was chosen in the version of ENO-EA which was presented in [4] and [29]. From a theoretical perspective all possibilities lead to the same approximation results, and therefore we only consider here the first one - interpolation of $\{z_{l-1}, z_{l+1}\}$ - which is the simplest.

Once $L_{k,l}$ is defined, we consider the polynomials p_l and p_r respectively defined from the stencils S_l and S_r defined by (43) and (44). The reconstruction $\mathcal{R}_h f$ is then defined on $C_{k,l}$ by p_l on the left side of $L_{k,l}$ and by p_r on the right side of $L_{k,l}$.

4. Approximation results

We are now ready to establish approximation results for the ENO-EA procedure when applied to piecewise C^s images f with piecewise C^2 edge discontinuities. More precisely, it is assumed that f and all its derivatives up to order s are uniformly over regions which are separated by discontinuity curves of uniform C^2 smoothness. These curves may however intersect at corners or T-junctions. Except at these isolated points, we have therefore

$$|\gamma''(t)| \leq \rho < +\infty \tag{59}$$

with ρ the maximum of the curvature. We always assume $1 \leq s$ as well as the natural limitation $s \leq 2m+1$ due to the order of accuracy of our method.

We first study the error $|f - \mathcal{R}_h f|$ locally on each cell $C_{k,l}$ in $L^p(C_{k,l})$ for $p \geq 1$. The error estimate depends on the position of the cell with respect to the edges and the corner or T-junctions. From this local study, we then derive global results on the sparsity of the multiscale representation and the approximation order of uniform and adaptive methods based on the ENO-EA procedure.

4.1 Local accuracy of the reconstruction

As announced in §2.5, the definition of $\mathcal{R}_h f$ on the cell $C_{k,l}$ is influenced by a set of cell $I_{k,l} = \{C_{k',l'} \ ; \ \sup\{|k-k'|, |l-l'|\} \leq M\}$, where M depends on the polynomial degree $2m+1$. We make the natural distinction between three types of cells:

1. Cells $C_{k,l}$ such that the influence set $I_{k,l}$ is not crossed by any edge. In such cells the function is regarded as globally C^s by the ENO-EA procedure. Therefore, regardless of the labeling of $C_{k,l}$, the procedure clearly gives the optimal $\mathcal{O}(h^s)$ approximation order

$$|f - \mathcal{R}_h f| \leq C h^s, \tag{60}$$

   where C is proportional to the L^∞ norm of the s-derivatives of f over $I_{k,l}$. This implies

$$\|f - \mathcal{R}_h f\|_{L^p(C_{k,l})} \leq C h^{s+\frac{2}{p}}. \tag{61}$$

2. Cells $C_{k,l}$ such that the influence set $I_{k,l}$ contains a corner or a T-junction. These types of discontinuities are not treated properly by the ENO-EA procedure which is tailored to *smooth* edge curves. In this case, one can only guarantee the $\mathcal{O}(1)$ approximation order by invoking the crude estimate

$$|f - \mathcal{R}_h f| \leq C \|f\|_{L^\infty} \tag{62}$$

   which holds since the procedure increases the L^∞ norm at most by a constant factor. This also implies

$$\|f - \mathcal{R}_h f\|_{L^p(C_{k,l})} \leq C h^{\frac{2}{p}}. \tag{63}$$

   These are the crudest estimates but they only occur at very few cells since corner and T-junctions are isolated points.

3. Cells $C_{k,l}$ such that the influence set $I_{k,l}$ is crossed by an edge but does not contain any corner or T-junction. We also assume that the edge does not re-enter $I_{k,l}$ as illustrated on Figure 1. For such cells, we shall prove that there is a significant improvement over the $\mathcal{O}(1)$ approximation order which would be achieved by a linear reconstruction method, say using the centered stencil for all cells.

Our main objective is therefore to establish local approximation results for the cells of the third type. Assuming that $C_{k,l}$ is such a cell, we consider several cases.

Case 1. The scale h is larger than a fixed multiple of the critical scale: $h \geq \kappa h_c$ with κ a constant to be fixed by the study of the next two cases. In this case, we use the fact that the method is at least first order accurate (exact for constant functions) in order to derive the crude estimate

$$|f - \mathcal{R}_h f| \leq C h \sup_{I_{k,l} \setminus E} |\nabla f| + \delta, \tag{64}$$

where $\delta = \sup_{E_{k,l}} |[f](t)|$. The condition $h \geq \kappa h_c$ means that

$$\kappa\delta \leq h(\sup_{I_{k,l}\setminus E} |\nabla f| + \delta \sup_{E_{k,l}} |\gamma''(t)|) \leq h(\sup_{I_{k,l}\setminus E} |\nabla f| + \delta\rho) \tag{65}$$

In particular, for $h \leq \frac{\kappa}{2\rho}$, we obtain an estimate $\delta \leq \frac{2}{\kappa} h \sup_{I_{k,l}\setminus E} |\nabla f|$, which combined with (64) yields the $\mathcal{O}(h)$ approximation order

$$|f - \mathcal{R}_h f| \leq Ch, \tag{66}$$

where C is proportional to the L^∞ norm of the gradient of f over $I_{k,l} \setminus E$. This implies

$$\|f - \mathcal{R}_h f\|_{L^p(C_{k,l})} \leq Ch^{1+\frac{2}{p}}. \tag{67}$$

Note that since $\frac{\kappa}{2\rho}$ is a fixed constant, we can also say that the $\mathcal{O}(h)$ order is valid for any $h < 1$ up to changing the constant in (66).

Case 2. $h \leq \kappa h_c$ and $C_{k,l}$ has been labeled G. This implies in particular that $C_{k,l}$ is not crossed by the edge. In the case where the reconstruction on $C_{k,l}$ was performed by a square stencil which only consists of G cells, we are also ensured that this stencil is not crossed by the edge and we therefore obtain on $C_{k,l}$ the optimal approximation order (60) similar to the cells of the first type. However, we need to address the case where such a stencil does not exists, and analyze the behavior of the stencil selection procedure based on the cost function (53). This is done in the lemma 10 below, which says that we have the $\mathcal{O}(h)$ approximation order

$$|f - \mathcal{R}_h f| \leq Ch\Big(\sup_{I_{k,l}\setminus E} |\nabla f| + \delta\rho\Big) \leq Ch, \tag{68}$$

which also implies (67) with C depending on ρ and on the L^∞ norm of f and it gradient over $I_{k,l} \setminus E$.

Case 3. $h \leq \kappa h_c$ and $C_{k,l}$ has been labeled HB or VB. Without loss of generality, we assume that the label is HB. The reconstruction $\mathcal{R}_h f$ is then defined as a piecewise polynomial function built from the cell-average data on the left and right stencils S_l and S_r, from both side of the estimated edge $L_{k,l}$. Since $C_{k,l}$ has been maintained HB after testing the stencils, we know from lemma 8 that the edge does not crosses the stencils S_l and S_r Two subcases have to be considered. In the first one, the edge does not cross the HB pair or triplet which contains $C_{k,l}$. Since the edge also does not crosses the stencils S_l and S_r, we are then ensured to obtain on $C_{k,l}$ the optimal approximation order (60) similar to the cells of the first type. In the second subcase, the edge crosses the HB pair or triplet. In this case, consider the line L which is tangent to E at the point which maximizes the jump over $I_{k,l}$, and for which we know by lemma 8 that $|\theta| \geq \theta^*$. We also denote by δ the size of the jump at the contact point. Our main observation will be that the estimated line $L_{k,l}$ is an accurate estimation of L in the sense that if $\{\overline{x}_{l-1}, \overline{x}_{l+1}\}$ denote the horizontal positions

of the centers of the segments of L crossing the rows $l-1$ and $l+1$, we then have

$$\max\{|x_{l-1}-\overline{x}_{l-1}|,|x_{l+1}-\overline{x}_{l+1}|\}\leq Ch^2\Big(\frac{\sup_{I_{k,l}\setminus E}|\nabla f|}{\delta}+\rho\Big)\leq C\frac{h^2}{\delta}. \quad (69)$$

This is proved in lemma 11 below. From this observation, and since the deviation between E and L is estimated by $C\rho h^2$, it follows that the deviation between E and $L_{k,l}$ is also less than $C\frac{h^2}{\delta}$. In turn, the region of $C_{k,l}$ separating E and $L_{k,l}$ over which the reconstruction uses the wrong stencil has area less than $C\frac{h^3}{\delta}$. On this region, we only have the crude estimate (64) which, since (35) holds, may be transformed into

$$|f-\mathcal{R}_h f|\leq C\delta. \quad (70)$$

On the rest of $C_{k,l}$ the optimal approximation order (60) is achieved. It follows that we have for all $p\geq 1$

$$\|f-\mathcal{R}_h f\|_{L^p(C_{k,l})}\leq C\Big(h^3\delta^{p-1}+h^{sp+2}\Big)^{\frac{1}{p}}\leq Ch^{\frac{2}{p}+\min\{\frac{1}{p},s\}}, \quad (71)$$

with C depending on ρ and on the L^∞ norm of f and it derivatives up to order s over $I_{k,l}$.

Clearly (67) and (71) improve over the approximation rate (63) on the corners and T-junctions. Under the assumption that $s\geq 1$, the worst estimate is (71) and it can be rewritten into

$$\|f-\mathcal{R}_h f\|_{L^p(C_{k,l})}\leq Ch^{\frac{3}{p}}. \quad (72)$$

We now prove the two announced lemmas.

Lemma 10 *In Case 2, the stencil selection based on the cost function (53) ensures that*

$$|f-\mathcal{R}_h f|\leq Ch\Big(\sup_{I_{k,l}\setminus E}|\nabla f|+\delta\rho\Big). \quad (73)$$

holds over $C_{k,l}$.

Proof: Let L be the line which is tangent to E at the point which maximizes the jump $|[f]|(t)$, and g the step image which takes on each side of L the corresponding limit values a and b of f at the contact point. We know that $C_{k,l}$ is also not crossed by L. It follows that

$$|f-g|\leq Ch\sup_{I_{k,l}\setminus E}|\nabla f| \quad (74)$$

over $C_{k,l}$. Denote by S be the stencil which is selected by the ENO procedure and by $\mathcal{R}_S$ the interpolation operator which uses the cell-average data over the

stencil S to reconstruct a polynomial of global degree $2m+1$. We therefore have $\mathcal{R}_h f = \mathcal{R}_S f$. It is also clear that for all function u, we have on $C_{k,l}$

$$|\mathcal{R}_S u| \leq C \max_{C_{n,q} \in S} |u_{n,q}|, \tag{75}$$

and in particular

$$|\mathcal{R}_S f - \mathcal{R}_S g| \leq C \max_{C_{n,q} \in S} |f_{n,q} - g_{n,q}| \leq Ch\Big(\sup_{I_{k,l} \setminus E} |\nabla f| + \delta\rho \Big), \tag{76}$$

where we have used (26) and the fact that $\mathcal{R}_S$ is linear once we have fixed the stencil S. Therefore, in order to prove (73), it suffices to prove that

$$|g - \mathcal{R}_S g| \leq Ch\Big(\sup_{I_{k,l} \setminus E} |\nabla f| + \delta\rho \Big). \tag{77}$$

Since L does not cross $C_{k,l}$, there also exists a square stencil $\tilde{S}$ containing it and which is not crossed by L. We define $\mathcal{C}(S,f)$ and $\mathcal{C}(S,g)$ as the cost function (53) for the stencil S with respect to the cell-averages of f and g respectively, and we define $\mathcal{C}(\tilde{S},f)$ and $\mathcal{C}(\tilde{S},g)$ in a similar manner. Since L does not cross $\tilde{S}$, we clearly have

$$\mathcal{C}(\tilde{S},g) = 0. \tag{78}$$

If L crosses S, we denote by α the area of the smallest of the two parts of S separated by L. Elementary yet tedious geometrical configurations show that

$$\mathcal{C}(S,g) \geq \delta \min(1, \frac{\alpha}{h^2}). \tag{79}$$

On the other hand we know that $\mathcal{C}(S,f) \leq \mathcal{C}(\tilde{S},f)$. Since according to (26) both $|\mathcal{C}(S,f) - \mathcal{C}(S,g)|$ and $|\mathcal{C}(\tilde{S},f) - \mathcal{C}(\tilde{S},g)|$ are estimated by $Ch\Big(\sup_{I_{k,l}\setminus E} |\nabla f| + \delta\rho\Big)$ with C some fixed constant, we necessarily have

$$2\delta \min(1, \frac{\alpha}{h^2}) \leq Ch\Big(\sup_{I_{k,l} \setminus E} |\nabla f| + \delta\rho \Big). \tag{80}$$

In the case where $\alpha \geq h^2$, we obtain that $\delta \leq Ch\Big(\sup_{I_{k,l}\setminus E} |\nabla f| + \delta\rho\Big)$, and so (73) is directly proved by invoking the crude estimate (64). In the case where $\alpha < h^2$, we denote by $\tilde{g}$ a function which is constant over S with the same value as g over the largest part of S separated by L. Clearly, we have $\mathcal{R}_S \tilde{g} = \tilde{g}$ on S and since $\alpha < h^2$ the cell $C_{k,l}$ has to be contained in the largest part of S separated by L so that $g = \tilde{g}$ on $C_{k,l}$. It follows that we have on $C_{k,l}$

$$\begin{aligned} |g - \mathcal{R}_S g| &= |\tilde{g} - \mathcal{R}_S g| \\ &= |\mathcal{R}_S \tilde{g} - \mathcal{R}_S g| \\ &\leq C \max_{C_{n,q} \in S} |\tilde{g}_{n,q} - g_{n,q}| \\ &\leq \delta \tfrac{\alpha}{h^2} \\ &\leq Ch\Big(\sup_{I_{k,l}\setminus E} |\nabla f| + \delta\rho\Big). \end{aligned}$$

which is (77). ◇

Lemma 11 *In Case 3, we have the estimate*

$$\max\{|x_{l-1}-\overline{x}_{l-1}|,|x_l-\overline{x}_l|,|x_{l+1}-\overline{x}_{l+1}|\}\leq Ch^2\Big(\frac{\sup_{I_{k,l}\setminus E}|\nabla f|}{\delta}+\rho\Big). \quad (81)$$

where $\{x_{l-1},x_l,x_{l+1}\}$ *and* $\{\overline{x}_{l-1},\overline{x}_l,\overline{x}_{l+1}\}$ *denote the horizontal positions of* L *and* $L_{k,l}$ *in the middle of the rows* $l-1$, l *and* $l+1$ *respectively.*

Proof: For notational simplicity, we prove the estimate for $|x_l-\overline{x}_l|$, the proof being identical for the rows $l-1$ and $l+1$. Let g the step image which takes on each side of L the corresponding limit values a and b of f at the contact point. According to the results of §2.2, we know that L and E both cross the row L inside the HB pair or triplet $(C_{q,l})_{q_l^-\leq q\leq q_l^+}$ which contains $C_{k,l}$. Recall that we have

$$x_l:=h\Big(q_l^-+\frac{(q_l^+-q_l^-+1)(c-b)}{a-b}\Big), \quad (82)$$

with

$$a:=f_{q_l^--1,l},\ \ b:=f_{q_l^++1,l}\ \text{ and }\ c:=\frac{1}{q_l^+-q_l^-+1}\sum_{q_l^-\leq q\leq q_l^+}f_{q,l}. \quad (83)$$

On the other hand, we have remarked that the edge reconstruction procedure exactly identifies L in the case where the cell-average data come from the step image g. Therefore we have

$$\overline{x}_l:=h\Big(q_l^-+\frac{(q_l^+-q_l^-+1)(\overline{c}-\overline{b})}{\overline{a}-\overline{b}}\Big), \quad (84)$$

with

$$\overline{a}:=g_{q_l^--1,l},\ \ \overline{b}:=g_{q_l^++1,l}\ \text{ and }\ \overline{c}:=\frac{1}{q_l^+-q_l^-+1}\sum_{q_l^-\leq q\leq q_l^+}g_{q,l}. \quad (85)$$

The lemma will therefore be proved if we can show that

$$\Big|\frac{c-b}{a-b}-\frac{\overline{c}-\overline{b}}{\overline{a}-\overline{b}}\Big|\leq Ch\Big(\frac{\sup_{I_{k,l}\setminus E}|\nabla f|}{\delta}+\delta\rho\Big). \quad (86)$$

For this, we write

$$\Big|\frac{c-b}{a-b}-\frac{\overline{c}-\overline{b}}{\overline{a}-\overline{b}}\Big|\leq\frac{|c-\overline{c}|+|\overline{b}-b|}{|\overline{a}-\overline{b}|}+\frac{|c-b|(|a-\overline{a}|+|\overline{b}-b|)}{|(\overline{a}-\overline{b})(a-b)|}. \quad (87)$$

Remark that $|\overline{a}-\overline{b}|=\delta$. Using (26), the first term on the right hand side is estimated by

$$\frac{|c-\overline{c}|+|\overline{b}-b|}{|\overline{a}-\overline{b}|}\leq\frac{Ch\Big(\sup_{I_{k,l}\setminus E}|\nabla f|+\delta\rho\Big)}{\delta} \quad (88)$$

which is the desired estimate. For the second term, we remark that since $h \leq \kappa h_c$, we have by (37)

$$|\overline{a} - a| + |\overline{b} - b| \leq C\kappa\delta, \tag{89}$$

and therefore, by choosing κ small enough

$$|\overline{a} - a| + |\overline{b} - b| \leq \frac{\delta}{2}, \tag{90}$$

which implies $|a - b| \geq \frac{\delta}{2}$. It follows, using both (26) and (37), that

$$\frac{|c-b|(|a-\overline{a}| + |\overline{b}-b|)}{|(\overline{a}-\overline{b})(a-b)|} \leq \frac{C|c-b|h\Big(\sup_{I_{k,l}\setminus E}|\nabla f| + \delta\rho\Big)}{\delta^2}. \tag{91}$$

Since obviously $|\overline{c} - \overline{b}| \leq \delta$, we obtain by (37) that

$$|c-b| \leq |\overline{c}-\overline{b}| + |c-\overline{c}| + |b-\overline{b}| \leq C\delta, \tag{92}$$

which combined with (91) gives the desired estimate. The proof of the lemma is therefore complete. ◇

4.2 Approximation and sparsity results

We can summarize as follow the error estimates which have been established for the ENO-EA method applied to a piecewise smooth image: cells of the first, second and third type respectively satisfy the local error estimates (61), (63) and (72).

Moreover for an image defined on the normalized square $[0,1]^2$ we can estimate the number of cells of each type by

$$N_1 \leq Ch^{-2}, \;\; N_2 \leq C \;\text{ and }\; N_3 \leq Ch^{-1}. \tag{93}$$

It then follows that the global L^p error is estimated by

$$\|f - \mathcal{R}_h f\|_{L^p} \leq C\Big(h^{sp} + h^2\Big)^{\frac{1}{p}} \leq Ch^{\min\{s,\frac{2}{p}\}}. \tag{94}$$

In particular for $s \geq 2$, we obtain an estimate

$$\|f - \mathcal{R}_h f\|_{L^p} \leq Ch^{\frac{2}{p}} \sim CN^{-\frac{1}{p}}, \tag{95}$$

where we have denoted by N the total number of cell-average which are used to build $\mathcal{R}_h f$. This should be contrasted with the linear reconstruction based on the centered stencil: with this method we can only rely on a $\mathcal{O}(1)$ approximation order for the cells of the second type, and we then obtain the estimate

$$\|f - \mathcal{R}_h f\|_{L^p} \leq Ch^{\frac{1}{p}} \sim CN^{-\frac{1}{2p}}. \tag{96}$$

The operator $\mathcal{R}_h$ still represents a uniform approximation, since it is based on the cell-average data sampled on a uniform grid. We are also interested in

comparing the ENO-EA procedure with the linear procedure in the context of adaptive approximation. One natural way of building such approximations is by using the multiscale framework which was described in §1.2: multiscale coefficients d_λ are defined as the error of prediction from level j - which corresponds to $h = 2^{-j}$ - to the next one. In the case where we used the linear procedure, the coefficients d_λ can be interpreted as the coordinates of the function f in a wavelet basis. This wavelet basis is usually normalized in L^2, which mean that we have normalized the d_λ in such a way that we have in particular

$$|d_\lambda| \leq \|f - \mathcal{R}_h f\|_{L^2(C_{k,l})} \tag{97}$$

when λ is associated to the cell $C_{k,l}$. We proceed to a similar normalization for the multiscale coefficients obtained with the ENO-EA procedure. Note however that since this is a non-linear procedure, these coefficients cannot be interpreted as the coordinates of f in a basis.

Adaptive approximations can be performed by thresholding the wavelet coefficients. This is also known as *best N-term approximation* which corresponds to keeping the N largest coefficients. When measuring the error in the L^p distance, this should be performed by sorting the coefficients in the order of magnitude where they appear when the wavelet is normalized in L^p, see [14, 18] for more details. Here we simply discuss the case $p = 2$, which correspond to the normalization that we have chosen.

As explained in the introduction, the rate N^{-s} of best N-term approximation in a basis is reflected by the amount of sparsity in the sequence (d_λ) in the sense that (1) is equivalent to (2). When using the linear reconstruction method in the computation of the multiscale coefficients, which corresponds to a decomposition in a biorthogonal wavelet bases, we know that the coefficients sequence is in general no sparser than $w\ell^1$. Consider now the coefficients sequence associated to the ENO-EA procedure. In view of (97) and of our previous findings, the coefficients at level j are estimated by $\mathcal{O}(2^{-3j})$, $\mathcal{O}(2^{-j})$ and $\mathcal{O}(2^{-\frac{3j}{2}})$ for cells of first, second and third type respectively (we assume here that $s \geq 2$ in order to ensure the first estimate). Using (93), we find that

$$\#\{\lambda\,;\,|d_\lambda| \geq \eta\} \leq C\Big(\sum_{2^{-3j}\geq\eta} 2^{2j} + \sum_{2^{-j}\geq\eta} 1 + \sum_{2^{-\frac{3j}{2}}\geq\eta} 2^j\Big) \leq C\eta^{-\frac{2}{3}}. \tag{98}$$

We therefore find that the coefficient sequence has the improved sparsity $w\ell^{\frac{2}{3}}$, similar to the coefficients in a curvelet frame [11, 10]. In view of (2), this suggests that the L^2 approximation rate of best N-term approximation should be $\mathcal{O}(N^{-1})$, which is also attained with curvelet frames (up to a logarithmic factor) or bandelet bases, and which improves over the rate $\mathcal{O}(N^{-\frac{1}{2}})$ attained by wavelet N-term approximation. *However this fact is not proved and we conjecture its validity as an open problem.* The difficulty is that the non-linear multiscale transform is not a decomposition in a basis, and the reconstruction error cannot be controlled in full generality by the ℓ^2 error on the coefficients. This brings out the natural question of the stability of nonlinear multiscale transforms, on which some partial results have been proved in [16].

It is possible however to introduce another adaptive algorithm based on the ENO-EA procedure for which the optimal approximation rates can be proved. The algorithm builds up a non-uniform partition of dyadic square cell by the following adaptive refinement procedure: we fix an accuracy parameter $\varepsilon > 0$, and starting from the coarsest resolution we iteratively split into four any cell $C_{k,l}$ of size h such that $\|f - \mathcal{R}_h\|_{L^p(C_{k,l})} \geq \varepsilon$. The algorithm terminates when the local L^p error is bounded by ε on each cell of the partition. Such adaptive refinement procedure are well understood in the case of linear reconstruction such as projection onto piecewise constant functions, see [19].

In our case, we denote by $\mathcal{A}_\varepsilon f$ the approximation which is defined by the nonlinear ENO-EA reconstruction on each cell of the adaptive partition. The number of degrees of freedom N_ε that describe $\mathcal{A}_\varepsilon$ is obviously proportional to the cardinality of the partition. We can estimate it by

$$N_\varepsilon \leq C\Big(\sum_{2^{-(s+\frac{2}{p})j} \geq \varepsilon} 2^{2j} + \sum_{2^{-\frac{2j}{p}} \geq \varepsilon} 1 + \sum_{2^{-\frac{3j}{p}} \geq \varepsilon} 2^j \Big) \leq C \max\{\varepsilon^{-\frac{p}{3}}, \varepsilon^{-\frac{2p}{sp+2}}\}. \quad (99)$$

By summing up $\|f - \mathcal{R}_h\|^p_{L^p(S)}$ over all cells S of the adaptive partition, we obtain that the global L^p error is bounded by

$$\|f - \mathcal{A}_\varepsilon f\|_{L^p} \leq \varepsilon (N_\varepsilon)^{\frac{1}{p}}. \quad (100)$$

In the case where $p = 2$ and $s \geq 2$, we therefore obtain

$$N_\varepsilon \leq C\varepsilon^{-\frac{2}{3}}, \quad (101)$$

and

$$\|f - \mathcal{A}_\varepsilon f\|_{L^2} \leq C\varepsilon^{\frac{2}{3}} \leq C N_\varepsilon^{-1}, \quad (102)$$

which is the optimal rate of approximation. A similar computation shows that for more general values of p, we obtain the rate $\mathcal{O}(N^{-\frac{2}{p}})$, which improves over the rate $\mathcal{O}(N^{-\frac{1}{p}})$ of adaptive approximation by wavelets.

The rates of approximation in L^p that we have obtained degenerate to $\mathcal{O}(1)$ - that is no convergence - when $p = \infty$, both with the uniform and adaptive method. This is no surprise, since we cannot expect convergence in L^∞ due to the presence of the edge discontinuity. As in the one dimensional case with ENO-SR, it is still possible to study convergence with the Hausdorff distance between graphs as a natural substitute to the L^∞ norm. Note that both uniform and adaptive method based on classical wavelet or other bases cannot converge in this metric, due to the presence of Gibbs phenomenon in the reconstruction near the discontinuity (however, additional processing can be performed in order to limitate this phenomenon, see [12]). In contrast, we can obtain convergence rates with the ENO-EA procedure, provided however that we assume that there is no corner or T-junctions, since Gibbs phenomenon might still appear in the vicinity of these points.

Consider first the uniform approximation $\mathcal{R}_h f$. Our local error analysis show that we have always $|f - \mathcal{R}_h f|$ controlled by a $\mathcal{O}(h)$ bound except in Case 3

of cells of the third type, for which we have an $\mathcal{O}(1)$ error in the region which corresponds to the mismatch of the real edge E by the line edge $L_{k,l}$. However we have seen that the deviation is controlled by $Ch^2\Big(\frac{\sup_{I_{k,l}\setminus E}|\nabla f|}{\delta}+\rho\Big)$, which is always $\mathcal{O}(h)$ due to (35). It follows that the Hausdorff distance satisfies

$$d(f,\mathcal{R}_h f)\leq Ch\sim CN^{-\frac{1}{2}}. \tag{103}$$

An adaptive approximation algorithm based on a splitting procedure can perform better, since we have in fact $|f-\mathcal{R}_h f|$ controlled by a $\mathcal{O}(h^s)$ on all the cells of first type. It follows that the Hausdorff distance ε is achieved with a partition of complexity

$$N_\varepsilon\leq C\Big(\sum_{2^{-sj}\geq\varepsilon}2^{2j}+\sum_{2^{-j}\geq\varepsilon}2^j\Big)\leq\max\{\varepsilon^{-\frac{2}{s}},\varepsilon^{-1}\}. \tag{104}$$

For $s\geq 2$, this gives the better rate

$$d(f,\mathcal{A}_\varepsilon f)\leq CN_\varepsilon^{-1}. \tag{105}$$

5. Numerical tests

In this section we perform numerical tests which illustrate the results obtained in the previous sections. We consider the case $m=1$ which corresponds to the use of bi-quadratic polynomials.

We use as test cases the 512×512 geometric images displayed in Figure 9. The first one represents an ideal step edge, the second one a piecewise constant image having straight edges with a $T-$ junction and the last one a piecewise smooth image having smooth and curved edges.

Figure 9: Geometric Test Images

Figure 10 displays the bad cells detected by the ENO-EA detection algorithm §2.2 at resolution level $j=8$, the finest level corresponding to the pixel resolution being $J=9$. As expected, these cells are exactly located along the edges. In the case of a real image, the first step of the detection algorithm

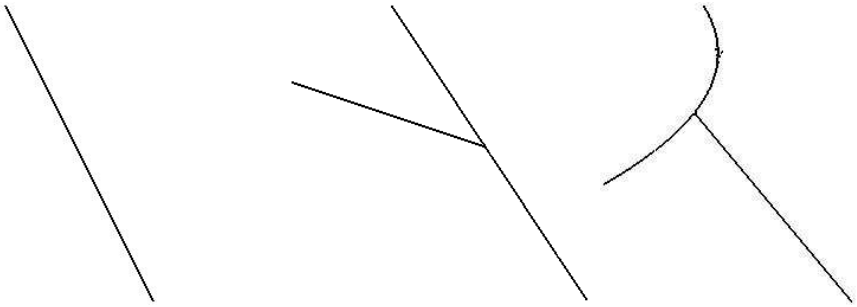

Figure 10: Bad Cells in the Vertical or Horizontal direction

tends to label as bad many cells which are not crossed by edges. However, the sequence of selection tests described in §2.3, 2.4 and 2.5 has the effect of eliminating these false alarms.

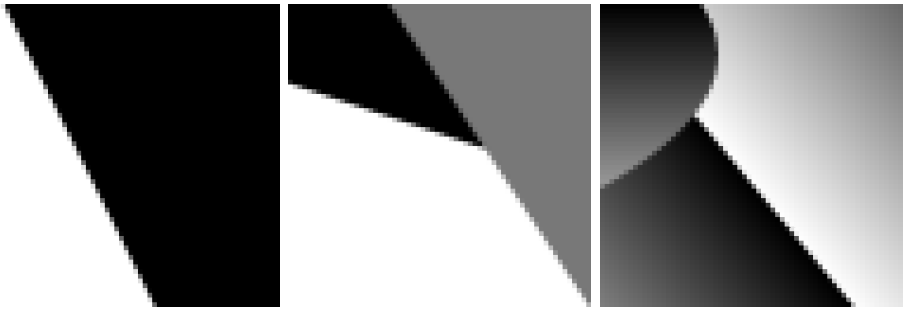

Figure 11: Coarse resolution images

We perform the reconstruction from the coarse cells of the three images at resolution $j = 7$. We display the corresponding low resolution images in Figure 11. Figure 12 displays the ENO-EA image reconstruction. As expected, the reconstruction is exact in the case of piecewise constant separated by line edges and highly accurate for curved edges. In contrast, Figure 13 displays the reconstruction based on the same cells, but using the linear reconstruction procedure (bi-quadratic polynomials with centered stencil). While the reconstruction is accurate in the smooth regions of the image, we notice that blurring and ringing artefacts are present on the edges.

Finally, we illustrate the sparsity of multiscale decomposition in the third geometric image, by displaying in Figure 14 the decreasing rearrangement of the coefficients sequence in logarithmic scale. The two curves correspond to the multiscale decompositions based on the linear and ENO-EA reconstruction procedure respectively. We observe three regimes:

1. The beginning of the curves corresponding to the 200 largest coefficients. These are typically coefficients corresponding to the coarsest scales for

Figure 12: Reconstruction results without adding details

Figure 13: Reconstruction results without adding details using linear methods

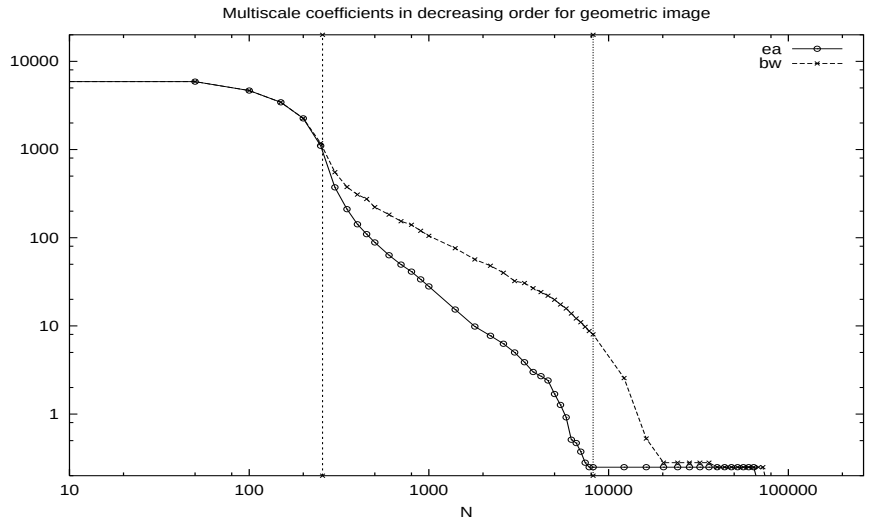

Figure 14: Decreasing rearrangement of the coefficients sequence for the geometric image with linear (bw) and ENO-EA (ea) decomposition

which the ENO-EA reconstruction is not more effective than the linear reconstruction since the scale is above the critical scale h_c and therefore the cells are too coarse for the algorithm to detect the geometry accurately.

2. The end of the curves corresponding to the smallest coefficients, with rank higher than 20000. These are typically the very small fine scale coefficients corresponding to the smooth regions, on which both the ENO-EA and linear reconstruction do as good.

3. The coefficients between rank 200 and 20000. These are typically the coefficients corresponding to the cells that meet the edges at sufficiently small scales so that the ENO-EA reconstruction is significantly better than the linear reconstruction. We observe that the two slopes in logarithmic scale are significantly different. A linear regression gives approximately slope -1.1 for the linear decomposition and -1.5 for the ENO-EA decomposition, which is in accordance with the improved sparsity result (98) obtained in the previous section.

Remark 4 *Since the multiscale transformation has the same hierarchical organization as the standard wavelet transform, its complexity remains of $\mathcal{O}(N) = CN$ complexity where N is the the number of pixels in the image. However, in the implementation of the method which was used in our numerical experiment, we observed that the multiplicative constant C was increased by a factor around 50 compared to a standard biorthogonal wavelet transform with the (5-7) filter pair, which is due to the fact that the linear filtering process is replaced by the more involved detection-selection-reconstruction process which was described in §2. We expect that this factor can be reduced by optimizing the implementation of the this process.*

Remark 5 *Our theoretical analysis and numerical experiments were conducted in the case of noiseless image data. In the case of an image corrupted by some additive noise, we have observed that the detection-selection-reconstruction mechanism is not significantly altered as long as the noise level is neglectable compared to the the amplitude of the true edge, but it might fail otherwise. Note that the noise level is meant here at the given scale of consideration, and therefore will be lower at coarser resolutions since the pixels have been produced by an averaging process. More precisely, for an additive white noise of variance σ^2 on each fine resolution pixel, the noise level σ at level J becomes $2^{j-J}\sigma$ at level $j < J$.*

6. Conclusions

In this paper, we present in detail the ENO-EA reconstruction procedure and prove that its approximation properties are better than those of wavelets in the case of piecewise smooth functions separated by piecewise C^2 edges, and similar to those of more advanced methods such as curvelets, bandlets, normal

meshes and wedgeprints in the case of the L^2 error. We also establish approximation results in L^p and in the Hausdorff metric. One of the specificity of our approach is that it retains exactly the same multiscale structure as classical wavelet transforms, the main change being in the local reconstruction procedure. Also, similar to curvelets and in contrast to bandlets and wedgeprints, we do not encode any geometrical information such as the orientation of the reconstructed edges, since this information is in some sense contained in the cell-average data which are used in the reconstruction process. Let us point out three intrinsic limitations of our approach:

1. The treatment of edges is done by reconstructing a sharp discontinuity. This means that our approach is not adapted to the treatment of blurred edges, in contrast to curvelets and bandlets which can treat these cases.

2. Similar to curvelets, wedgeprints and normal meshes, our approximation rates are optimal for C^2 edges, yet sub-optimal for smoother edges, in contrast to bandlets. This is due to the fact that we approximate the edge by a line. It is theoretically possible to develop a similar approach with the line replaced by a polynomial piece but the identification procedure for this piece is then much more complex.

3. Although observed in practical numerical experiments, the stability of the multiscale transform associated with the ENO-EA procedure does not hold in full generality.

From a more applied perspective, compression algorithms based on the ENO-EA procedure have already been introduced in [4] and [29]. The optimal encoding strategy for the multiscale coefficients is still the object of current research. Other natural applications that will be investigated are zooming (by which we mean deriving a high resolution image from coarse resolution data) and geometrical interface reconstruction in numerical simulation of PDE's.

Acknowledgment: This work was partially supported by EU-IHP HPRN-CT-2002-00286 and MTM 2005-07214.

References

[1] S. Amat, F. Arandiga, A. Cohen and R. Donat, *Tensor product multiresolution with error control*, Signal Processing 82, 587-608, 2002

[2] S. Amat, F. Arandiga, A. Cohen, R. Donat, G. Garcia and M. Von Oehsen, *Data compression with ENO schemes - a case study*, Appl. Comp. Harm. Anal. 11, 273-288, 2001.

[3] F. Arandiga, A. Cohen, R. Donat and N. Dyn, *Interpolation and approximation of piecewise smooth functions*, SIAM J. Numer. Anal. 43-1, 41-57, 2005.

[4] F. Arandiga, A. Cohen, M. Doblas and B. Matei, *Edge adapted nonlinear multiscale transforms for compact image representation*, IEEE Int. Conf. Image Proc., Barcelona 2003, 701-704.

[5] F. Arandiga and R. Donat, *Nonlinear multiscale decompositions: the approach of A. Harten*, Numerical Algorithms 23, 175-216, 2000.

[6] R. Baraniuk, R. Claypoole, G. M. Davis and W. Sweldens, *Nonlinear wavelet transforms for image coding*, Proc. 31st Asilomar Conference, 1997.

[7] R. Baraniuk, R. Claypoole, G. M. Davis and W. Sweldens, *Nonlinear wavelet transforms for image coding via lifting*, IEEE Trans. Image Proc. 12, 1449-1459, 2003.

[8] R. Baraniuk, M. Janssen and S. Lavu, *Multiscale approximation of piecewise smooth two-dimensional functions using normal triangulated meshes*, ACHA 19, 92–130, 2005.

[9] R. Baraniuk, H. Choi, J. Romberg and M. Wakin, *Wavelet-domain approximation and compression of piecewise smooth images*, IEEE Transactions on Image Processing, to appear 2006.

[10] E. Candes and D. L. Donoho, *New tight frames of curvelets and optimal representations of objects with smooth singularities*, Technical Report, Stanford University, 2002.

[11] E. Candes and D. L. Donoho, *Curvelets and curvilinear integrals*, J. Approx. Theory. 113, 59–90, 2000.

[12] E. Candes, J. L. Starck and D. L. Donoho, *Very High Quality Image Restoration by Combining Wavelets and Curvelets*, in Wavelet Applications in Signal and Image Processing IX, A. Aldroubi, A. F. Laine, M. A. Unser eds., Proc. SPIE 4478, 2001.

[13] T. Chan and H. M. Zhou, *ENO-Wavelet transforms for piecewise smooth functions*, SIAM J. Numer. Anal. 40-4, 1369–1404, 2002.

[14] A. Cohen, *Numerical Analysis of Wavelet Methods*, Elsevier, 2003.

[15] A. Cohen, W. Dahmen, I. Daubechies and R. DeVore, *Tree approximation and optimal encoding*, Appl. Comp. Harm. Anal. 11, 192-226, 2001.

[16] A. Cohen, N. Dyn and B. Matei, *Quasilinear subdivision schemes with applications to ENO interpolation*, Appl. Comp. Harm. Anal. 15, 89-116, 2003.

[17] L. Demaret, N. Dyn, M. Floater and A. Iske, *Adaptive thinning for terrain modelling and image compression*, in Advances in Multiresolution for Geometric Modelling, N.A. Dodgson, M.S. Floater, and M.A. Sabin (eds.), Springer-Verlag, Heidelberg, 321-340, 2005.

[18] R. DeVore, *Nonlinear Approximation*, Acta Numerica 7, 1998, 51-150.

[19] R. DeVore and X. M. Yu *Degree of adaptive approximation*, Math. Comp. 55, 1990, 625-635.

[20] M. N. Do and M. Vetterli, *The contourlet transform: an efficient directional multiresolution image representation*, IEEE Trans. on Image Processing 14-12, 2091-2106, 2005.

[21] Donoho, D. L. (1993), *Unconditional bases are optimal bases for data compression and for statistical estimation* , Appl. Comp. Harm. Anal.1, 100-115.

[22] N. Dyn, Michael Floater and A. Iske, *Adaptive thinning for bivariate scattered data*, J. of Comp. and Appl. Math. 145, 505-517, 2002.

[23] A. Harten, *ENO schemes with subcell resolution*, J. Comp. Phys. 83, 148-184, 1989.

[24] A. Harten, *Discrete multiresolution analysis and generalized wavelets*, J. Appl. Numer. Math. 12, 153-192, 1993.

[25] A. Harten, *Multiresolution representation of data: general framework*, SIAM J. Numer. Anal. 33, 1205-1256, 1996.

[26] E. Le Pennec and S. Mallat, *Sparse geometrical image approximation with bandelets*, IEEE Trans. on Image Processing 14-4, 423-438, 2005.

[27] E. Le Pennec and S. Mallat, *Bandelet image approximation and compression*, submitted 2004.

[28] S. Mallat, *A wavelet tour of signal processing*, Academic Press, 1998.

[29] B. Matei, *Méthodes multirésolution non-linéaires - Applications au traitement d'image*, PhD dissertation, Université Paris VI, 2002.

[30] B. Matei, *Smoothness characterization and stability in nonlinear multiscale framework: theoretical results.* Asymptot. Anal. 41, no. 3-4, 2005, 277–309.

[31] M. Vetterli, P. Marziliano and T. Blu. *Sampling signals with finite rate of innovation*, IEEE Trans. on Signal Proc. 50-6, 2002, 1417-1428 .

Francesc Arandiga
Dept. Matematica Aplicada
Universitat de Valencia
C/ Dr. Moliner, 50
Burjasot, (Valencia) Spain
e–mail: `arandiga@uv.es`
www: `http://gata.uv.es/∼arandiga`
Tel: 34-96-3544727, Fax: 34-96-3544085

Albert Cohen
Laboratoire Jacques-Louis Lions
Université Pierre et Marie Curie
175 Rue du Chevaleret, 75013 Paris
France
e–mail: cohen@ann.jussieu.fr
www: http://www.ann.jussieu.fr/∼cohen
Tel: 33-1-44277195, Fax: 33-1-44277200

Rosa Donat
Dept. Matematica Aplicada
Universitat de Valencia
C/ Dr. Moliner, 50
Burjasot, (Valencia) Spain
e–mail: donat@uv.es
www: http://gata.uv.es/∼donat
Tel: 34-96-3544727, Fax: 34-96-3544085

Nira Dyn
School of Mathematical Sciences
Tel Aviv University
Ramat Aviv 69987
Israel
e–mail: niradyn@math.tau.ac.il
www: http://www.math.tau.ac.il/∼niradyn
Tel: 972-3-6409615, Fax:972-3-6409357

Basarab Matei
Laboratoire Analyse Géométrie et Applications
Institut Galilée Université Paris Nord
99, avenue Jean-Baptiste Clément
93430 - Villetaneuse
France
e–mail: matei@math.univ-paris13.fr
www: http://www-math.univ-paris13.fr/∼matei
Tel: 33-1-49403571, Fax: 33-1-49403568